GEOPHYSICS, VOL. 77, NO. 6 (NOVEMBER-DECEMBER 2012); P. P45–P56, 19 FIGS., 1 TABLE.
10.1190/GEO2012-0037.1

Nongeometrically converted shear waves in marine streamer data

Guy Drijkoningen[1], Nihed el Allouche[1], Jan Thorbecke[1], and Gábor Bada[2]

ABSTRACT

Under certain circumstances, marine streamer data contain nongeometrical shear body wave arrivals that can be used for imaging. These shear waves are generated via an evanescent compressional wave in the water and convert to propagating shear waves at the water bottom. They are called "nongeometrical" because the evanescent part in the water does not satisfy Snell's law for real angles, but only for complex angles. The propagating shear waves then undergo reflection and refraction in the subsurface, and arrive at the receivers via an evanescent compressional wave. The required circumstances are that sources and receivers are near the water bottom, irrespective of the total water depth, and that the shear-wave velocity of the water bottom is smaller than the P-wave velocity in the water, most often the normal situation. This claim has been tested during a seismic experiment in the river Danube, south of Budapest, Hungary. To show that the shear-related arrivals are body rather than surface waves, a borehole was drilled and used for multicomponent recordings. The streamer data indeed show evidence of shear waves propagating as body waves, and the borehole data confirm that these arrivals are refracted shear waves. To illustrate the effect, finite-difference modeling has been performed and it confirmed the presence of such shear waves. The streamer data were subsequently processed to obtain a shear-wave refraction section; this was obtained by removing the Scholte wave arrival, separating the wavefield into different refracted arrivals, stacking and depth-converting each refracted arrival before adding the different depth sections together. The obtained section can be compared directly with the standard P-wave reflection section. The comparison shows that this approach can deliver refracted-shear-wave sections from streamer data in an efficient manner, because neither the source nor receivers need to be situated on the water bottom.

INTRODUCTION

In recent years, serious efforts have been made to obtain seismic shear-wave information from the shallow subsurface. Shear-wave properties are more directly related to the soil strength than compressional-wave properties. Therefore, shear-wave information has a direct impact on activities such as building structures on, or in, the subsurface, or retrieval of coarse sand for land reclamation and building projects.

On land, particular effort has been put into shear waves when the top layers are of the soft-soil type (e.g., Ghose and Goudswaard, 2004). Shear waves are not sensitive to the pore contents of the rock or soil, giving advantages over P-wave seismic surveys, especially when target depths are above the water table and/or in the "weathered" layer. Additionally, for soil characterization the shear-wave velocity can be used as an indicator of soil type, such as peat ($c_S \approx 70$ m/s), clay ($c_S \approx 110$ m/s), or sand ($c_S \approx 200$–300 m/s). Therefore, this type of wave is often used in geotechnical surveys. In many areas of the world, obtaining local shear-wave velocities from a direct borehole measurement is standard practice.

Shear-wave information is more difficult to obtain offshore. The stakes are higher because building offshore is much more expensive than onshore. In many offshore areas, site investigations, including seismic surveying, are required. In those cases, P-wave reflection data are commonly obtained, using sources such as the boomer, sparker, and chirp systems. P-wave reflection images show the structure of the subsurface (sometimes superbly) and show areas where shallow gas is present. However, P-wave data are not good for indicating what type of soil one is dealing with. On the other hand, acquiring shear-wave data through excitation and recording

Manuscript received by the Editor 31 January 2012; revised manuscript received 7 May 2012; published online 12 October 2012.
[1]Delft University of Technology, Department of Geoscience and Engineering, Delft, The Netherlands. E-mail: g.g.drijkoningen@tudelft.nl; n.elallouche@tudelft.nl; J.W.Thorbecke@tudelft.nl.
[2]TXM Oil and Gas Exploration Ltd., Budapest, Hungary. E-mail: gabor.bada@txm.hu.

at the water bottom is often quite cumbersome, rather slow, and therefore expensive. In this article, we present evidence that contact with the water bottom is not really needed to obtain good shear body wave information from the subsurface.

During the last decade, successful results have been obtained using surface/Scholte waves to infer the shear-wave properties of the subsurface (Park et al., 1999; Kaufmann et al., 2005; Park et al., 2005). With this approach, surface-wave arrivals are selected, analyzed in terms of their dispersion characteristics, and inverted for a shear-wave model of the shallow subsurface. However, these arrivals are related to the surface and the very shallow subsurface, depending on the wavelength and how many propagation modes can be picked and inverted. A key characteristic of a surface wave is that it decays exponentially with depth. This is in contrast with body waves.

Seismic surveyors performing shallow seismic investigations with a low-frequency source, such as an airgun, see slow low-frequency events within their records (Figure 1). The main low-frequency arrivals can be interpreted as surface/Scholte waves. Also, faster low-frequency events can be seen, and these are the focus of this study. It is well known that P-wave energy can give rise to a transmitted S-wave at the water bottom via geometrical conversion, although the transmission coefficient is small (see, e.g., Allouche et al., 2008). However, nongeometrical conversion can take place too. A nongeometrical arrival is an arrival that includes an evanescent-wave "path". It does not satisfy Snell's Law when only real angles are allowed; it does so only when complex angles are considered. The imaginary part of the angle is associated with an evanescent wave. In Figure 2, a schematized drawing of the main events in a fluid-solid configuration is given. It is assumed that the shear-wave velocity in the solid is (much) smaller than the P-wave velocity in the fluid. A source is situated in the fluid, just above the fluid-solid interface. The source generates P-waves in the water and the interface generates the usual arrivals, such as a P-wave reflection and transmission. A conversion to an S-wave occurs too, a geometrical conversion for which Snell's law with real angles holds. It can be seen that the range of angles for geometrical conversion is limited. The important point to make here is that this configuration also generates a nongeometrical arrival, as indicated in the figure. A much larger range of angles is captured by the nongeometrical conversion.

Recently, Allouche et al. (2010, 2011) have shown that these nongeometrically converted shear waves are clearly observable in data from a marine environment. They used data from water-bottom receivers in a shallow canal to demonstrate this statement, and they modeled seismic data to verify whether the observed response was consistent with the simulated response. On land, evanescent P-waves are discussed by Daley and Hron (1983), who first used the term S*-wave to refer to nongeometrically converted waves. Subsequently, their findings found theoretical support by a Cagniard-de Hoop analysis by Drijkoningen and Chapman (1988). In high-resolution seismic exploration data on land, Roth and Holliger (2000) also describe the occurrence of such a wave, and support their interpretation by a Cagniard-de Hoop analysis.

These first results were used to test a very promising approach for shear-wave surveying in shallow underwater environments. We describe an experiment conducted on the river Danube, near the village of Kulcs in Hungary. In this experiment, 4C borehole and streamer data were simultaneously recorded. Recording data in a borehole shows convincingly that shear waves are propagating in the mode of body waves, and not of surface waves. The data from the borehole also show what types of arrivals are present in the streamer data. Modeling has been done for the borehole and the streamer data to show that these arrivals are consistent with this interpretation. The modeling uses elastic-wave theory via the finite-difference (FD) method. As a second step, starting from the streamer field data, the shear-wave arrivals are enhanced and imaged via a special processing sequence. The resulting product is a shear-wave refraction section. This shear-wave refraction section is finally compared to a P-wave reflection section, obtained with a standard reflection-data processing sequence from the high-frequency portion of the same data set. After some discussion of the assumptions, implications, consequences, and drawbacks of the approach, the obtained results are summarized in the conclusions.

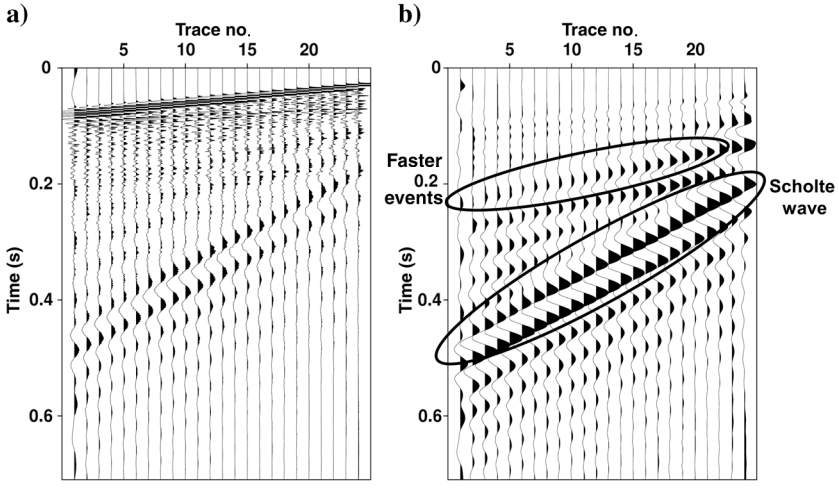

Figure 1. Real streamer record, showing low-frequency shear-wave related events. (a) Full record; (b) low-pass filtered record. Trace distance is 3.125 m.

EXPERIMENTS ON THE RIVER DANUBE NEAR KULCS, HUNGARY

Aims of the experiments

To show that shear-body-wave information is present in, and can be imaged from, streamer data, the main aims of these seismic experiments are to show that:

- Shear motion in the mode of body waves is generated,
- Shear-wave arrivals are also present in streamer data, and
- The shear body-wave information can be imaged from the streamer data.

During recent years, many surface-wave recordings have been taken at the water bottom, Therefore, the first aim of the experiment was to show unequivocally that events are body waves and not surface waves. To that end, seismic data from a borehole were essential.

The next aim was to show that these shear body waves are also present in streamer data. Allouche et al. (2011) showed that a single airgun in the water can generate shear waves, as long as the airgun is near (smaller than a quarter of the dominant P-wavelength) the water bottom. In that case, the evanescent P-wave in the water converts to a propagating S-wave in the bottom layer. The presence of these shear waves was shown using an "ocean-bottom" cable. What was not shown is that these waves can also be detected by a streamer of hydrophones in the water, via an evanescent P-wave in the water. This requires the streamer to be near the water bottom (<quarter of dominant P-wavelength).

Complementary information

The site for the experiments was chosen so that the survey could obtain valuable information on the subsurface. The area is part of the Pannonian basin; see, e.g., Bada and Horváth (2001), and Dombrádi et al. (2008). The experimental site was on the river Danube near a village called Kulcs, some 50 km south of Budapest. A fault zone known as the "Mid-Hungarian Lineament" crosses the area (Csontos and Nagymarosy, 1998). Near the village of Kulcs, a seismically active fault, being part of this Mid-Hungarian Lineament, crosses the river Danube. It connects to a fault seen on seismic images of a parallel branch of the river Danube (see Figure 4 in Csontos and Nagymarosy, 1998).

For our experiments and interpretations, it was important to know the lithology of the first 100 m of the subsurface. The rocks are of Late-Miocene and Pliocene age, consisting of sands and shales, mainly in "layered-cake" structures. The burial history of the formations has been such that they have not become solid rocks and samples mostly fell apart.

Although the area had been chosen also for its geologic significance, its main advantage was its suitability for the testing and validation of the retrieval of shear body waves. The experiment required a stretch of the Danube where the current was not too strong so that a borehole could be drilled safely. In addition, the river bottom needed to be rather flat over the survey area. A small Seistec® survey was used to decide on the precise location of the borehole.

A week before the seismic surveying started, a borehole of 85 m was drilled within the Danube. Because it was not possible to get proper rock samples from the borehole due to crumbling, only a description of the drill cuttings was available; Figure 3 shows a simplified lithological column used for comparison with the seismic results. The depths obtained from this description are not very accurate, but are indicative.

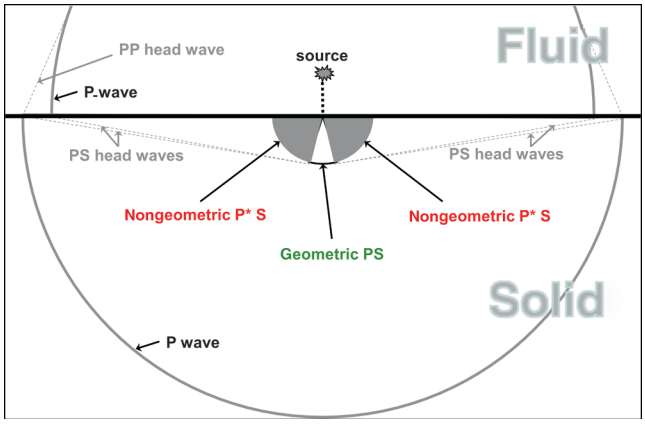

Figure 2. Schematic drawing of snapshots for Model 1, showing different events, and in particular the area where the nongeometric P*S-wave occurs. Model: $c_{S,\text{solid}} < c_{\text{fluid}}$ and $c_{\text{fluid}} < c_{P,\text{solid}}$.

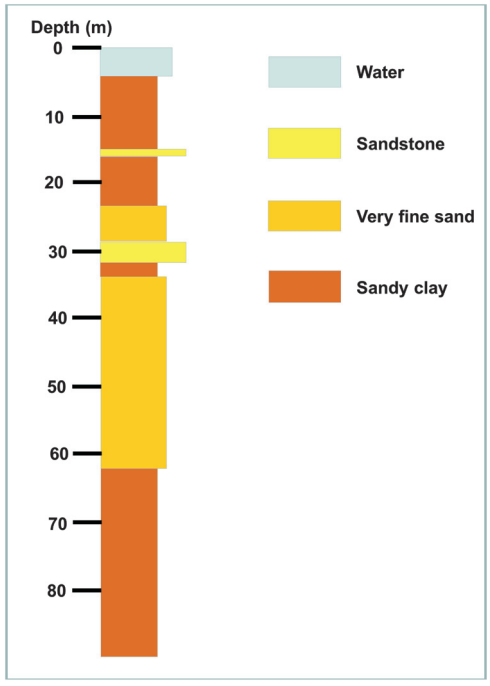

Figure 3. Lithological column at borehole, based on drill cuttings and simplified for comparison with seismic sections (layers < 1 m omitted; gradations of sand in clay combined in one classification of sandy clay).

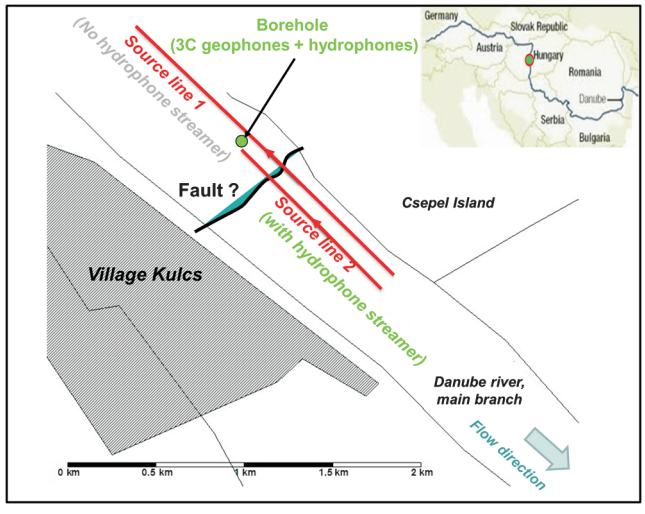

Figure 4. Plane view of experimental setup for shear-wave recordings near the village of Kulcs, Hungary. The inset (top right) shows the location of Kulcs on the regional map. Green: receiver-related. Red: source related. Coordinates of borehole: 18°55′18.91″ E, 47° 03′51.22″ N.

Seismic data acquisition

A 10 cu-inch airgun was used as source. Because S-waves propagate in the shallow subsurface (much) slower than P-waves, comparable resolution can be obtained by using (much) lower frequency sources. As had been shown by Allouche et al. (2011), such an airgun gives good shear-wave data.

For the recordings, a 48-channel Stratavisor® was used, together with two 24-channel Geodes® connected to laptops. Relatively long records (two seconds) had to be taken for these shallow depths because the slow shear waves needed to be recorded. The airgun was triggered every four or five seconds. Because the spatial sampling of the source needed to be as small as possible, the boat sailed against the current (speed, 4 m/s) and had an effective sail speed of ~1 m/s. The shot spacing was therefore approximately 4.5 m.

All systems were recording global positioning system (GPS) times. GPS coordinates of the airgun source were measured from a little boat 3 m behind the airgun using a Trimble® system.

In the borehole, a 3C tool was used, clamped with an air hose to the borehole wall; the tool consisted of eight elements at a spacing of 1 m. To cover the full depth range of the borehole, 14 boat tracks were acquired; for each track the 3C tool was brought up 7 m, starting from the bottom. A hydrophone tool was also used in the borehole, making the borehole measurements 4C, and consisted of 12 hydrophones at a spacing of 1 m. Surface recordings were performed with a hydrophone streamer behind the boat consisting of 24 hydrophone groups (four hydrophones per group) spaced at 3.125 m.

The acquisition geometry is shown in Figure 4. Two source lines are indicated: one is split-spread and one is end-on spread. For the borehole recordings, split-spread data were shot (source line one in Figure 4). For this source line, the hydrophone streamer data were not recorded (channels were used for the ocean-bottom cable (OBC) as in Allouche et al., 2011). The data from the hydrophone streamer were only recorded in the end-on mode (source line two in Figure 4).

BOREHOLE DATA

To distinguish between surface waves and shear waves, data from a borehole are essential. In Figure 5, three vertical-component common-receiver gathers (CRGs) from the borehole are shown. Their depths were chosen to illustrate the amplitude decay of the surface wave. These three CRGs were obtained from three different passes of the source boat.

The shallowest recording at 10 m depth as shown in Figure 5a is quite noisy. This had been observed on the OBC as well (Allouche et al., 2010), which was initially interpreted as bad coupling, but the borehole sensors are well-coupled to the borehole wall, so the noise was therefore interpreted as generated by the river flow (~3 m/s). The main arrivals are the direct P-waves with a velocity of ~1600 m/s and the Scholte-wave with a velocity of 240 m/s. A spectral analysis of the P-wave shows a significant amplitude roughly between 50 and 300 Hz. An analysis of the Scholte wave gives significant amplitudes roughly between 10 and 30 Hz (associated with a wavelength of 24 and 8 m, respectively). Another observation on the Scholte wave is that it does not show any dispersion. A faster fainter shear-related arrival, seeming to come from the deeper subsurface, can also be seen with a velocity of ~400 m/s; the frequency contents is similar to the Scholte wave. With a 3C geophone at the depths of 25 m and 40 m (Figure 5b and 5c, respectively), the data become less noisy and more easily interpretable; the noise from the river flow has largely disappeared. The arrival of the 240 m/s wave has completely disappeared at 40 m depth, as expected for the surface wave (with a rule of thumb that the maximum depth is a half the longest wavelength of the

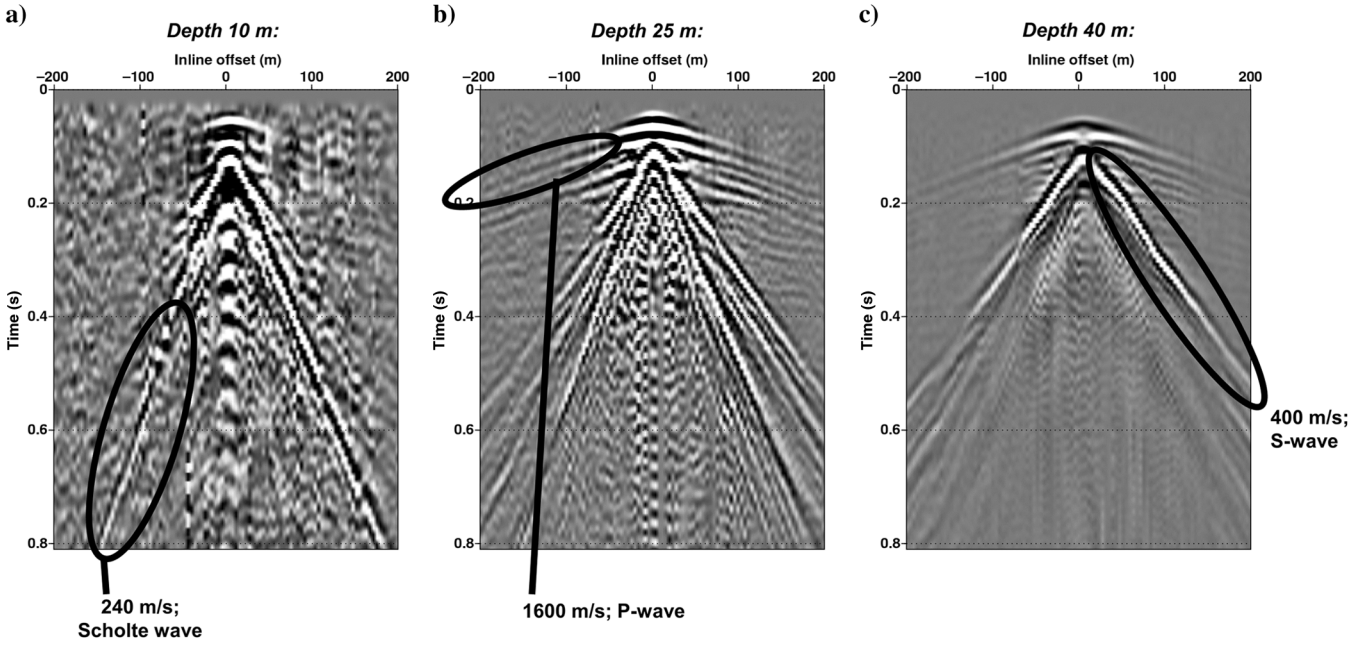

Figure 5. Vertical component of particle-velocity data from borehole recordings at (a) 10 m depth, (b) 25 m depth, and (c) 40 m depth. The velocity and interpretation of prominent events are indicated. Note: Some crossline offset between source and borehole is present, and therefore the P-wave and shear-wave-related events do not start at $t = 0$ for zero inline offset. (Preprocessing applied: regularization, low-pass filtering, and prediction-error filtering).

interface wave [Caiti et al., 1994]). Only the arrival with a 400 m/s velocity remains. This faint arrival recorded at the shallow-depth (Figure 5a) is therefore a body wave. This arrival can be interpreted as a P*S-wave, i.e., an evanescent P-wave, converted to a propagating S-wave.

MODELING THE BOREHOLE RECORD

When these observations were made, the question arose of whether this type of behavior could be modeled to determine whether our interpretations were consistent with elastic-wave theory. The FD method was chosen because of the ability to generate snapshots, but also because a laterally varying structure needed to be modeled — in our case, a fault (see below). A lossless elastic 2D scheme is used, as described in Virieux (1986), with the implementation as described in Thorbecke and Draganov (2011). With this approach, the scheme, a fourth-order scheme in space and second-order scheme in time is applied, employing a staggered and explicit grid.

The use of a 2D model implies that crossline offset present in the real data cannot be modeled. Initially, a 1D model was used, with the aim to synthesize the behavior of the P*S-wave as seen in the real borehole data. The model is 1200 m wide (x-direction) by 650 m deep (z-direction), divided into grid blocks of 0.5×0.5 m; the top layer (water) has a free surface on top. The borehole is at $x = 0$ m in this model. The size of the model is taken such that artificial reflections from the sides of the model do not interfere with the arrivals of interest. This simple model, called "Model 1," is shown in Figure 6. It includes a water layer of 4 m at the top, similar to the real survey, and a half-space with a constant velocity, also similar to observed in the real data. A single shot was generated. Because the model is horizontally invariant, the shot was replicated to simulate a complete survey with a source spacing of 4 m. A minimum-phase wavelet was used, created by filtering a delta-pulse with a minimum-phase Butterworth bandpass filter with frequency content similar to that observed in the data, with the dominant frequency around 26 Hz.

To appreciate the shear-wave motion generated in Model 1, we used the snapshot feature of the FD method. The snapshots should show the main body-wave arrivals as shown schematically in Figure 2, that was made roughly consistent with the velocities as used in the modeling ($c_S = 240$ m/s and $c_P = 1600$ m/s in the solid). Three different snapshots are shown in Figure 7, which illustrate different features. The first snapshot shows the P-wave as a faint fast "low-frequency" event at around 100 m from the source location. As can be observed from that P-wave event, the wavelength is large compared to the wavelengths of the S-converted P-wave at

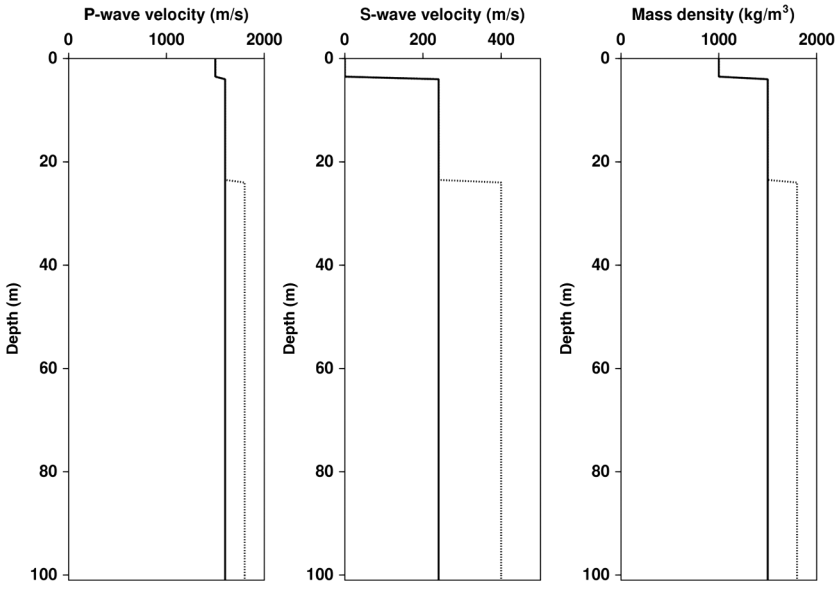

Figure 6. Models for V_P, V_S, and ρ used as input for finite-difference modeling. Solid: Model 1. Dotted: Model 2. Note: Models 1 and 2 coincide in the upper 24 m.

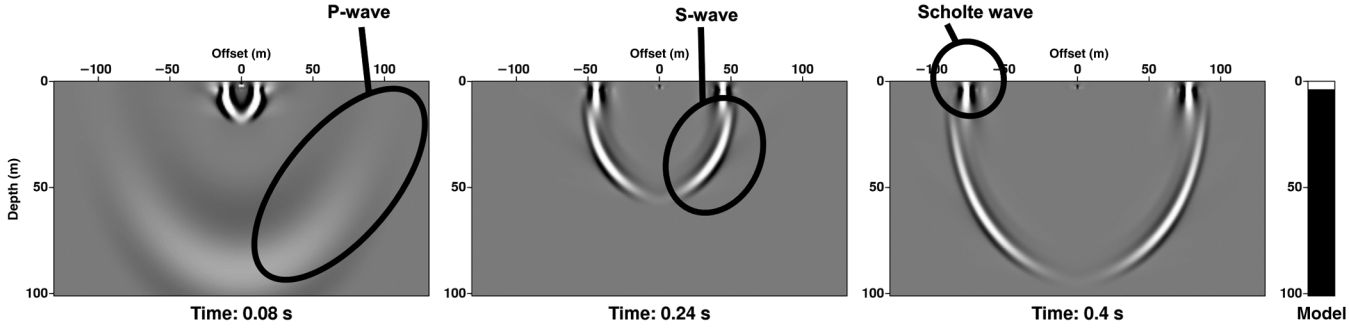

Figure 7. Snapshots of particle-velocity wavefields, showing evanescent P-waves becoming propagating (body) S-waves and Scholte waves. Note the model on the right side where the top (white) indicates the water layer.

around 20 m from the source location. This shows that the water bottom, for these frequencies, is close enough to the airgun source to allow the evanescent P-wave to become a propagating S-wave in the water bottom. (It is perhaps noteworthy that the FD modeling represents the evanescent wave very well. To the best of our knowledge, this has not been reported anywhere in the literature.)

In the next snapshot in Figure 7b, the evolution of the S-wave in the subsurface can be seen. Near the surface, a distinction between the surface (Scholte) wave and the S-wave becomes observable. The distinction is well-developed in the third snapshot, where the surface wave can be seen as well as the S-wave. It is also clearly observable that the surface wave dampens out with depth.

Associated with these snapshots, three CRG records at different depth levels are plotted to simulate a borehole setting (Figure 8). At a shallow depth of 10 m, the surface wave is dominant (and there is a faint faster P-wave). At a greater depth of 25 m, the S-wave is more pronounced in amplitude than the surface wave, but the surface wave can still be seen tailing the S-wave at larger offsets and times, as indicated in Figure 8b. At the greatest depth of 40 m (Figure 8c), only the S-wave is visible and the surface wave is too small in amplitude to be observable.

To simulate refracted and/or reflected S-waves as observed in the real borehole data, an extra layer in the subsurface was added to the previous model. This is called Model 2, and is also shown in Figure 6. To better simulate the borehole data, a time correction was applied to the synthetic data to include the extra time due to the crossline offset present in the real data. The simulated borehole data for two different borehole depth levels are shown in Figure 9.

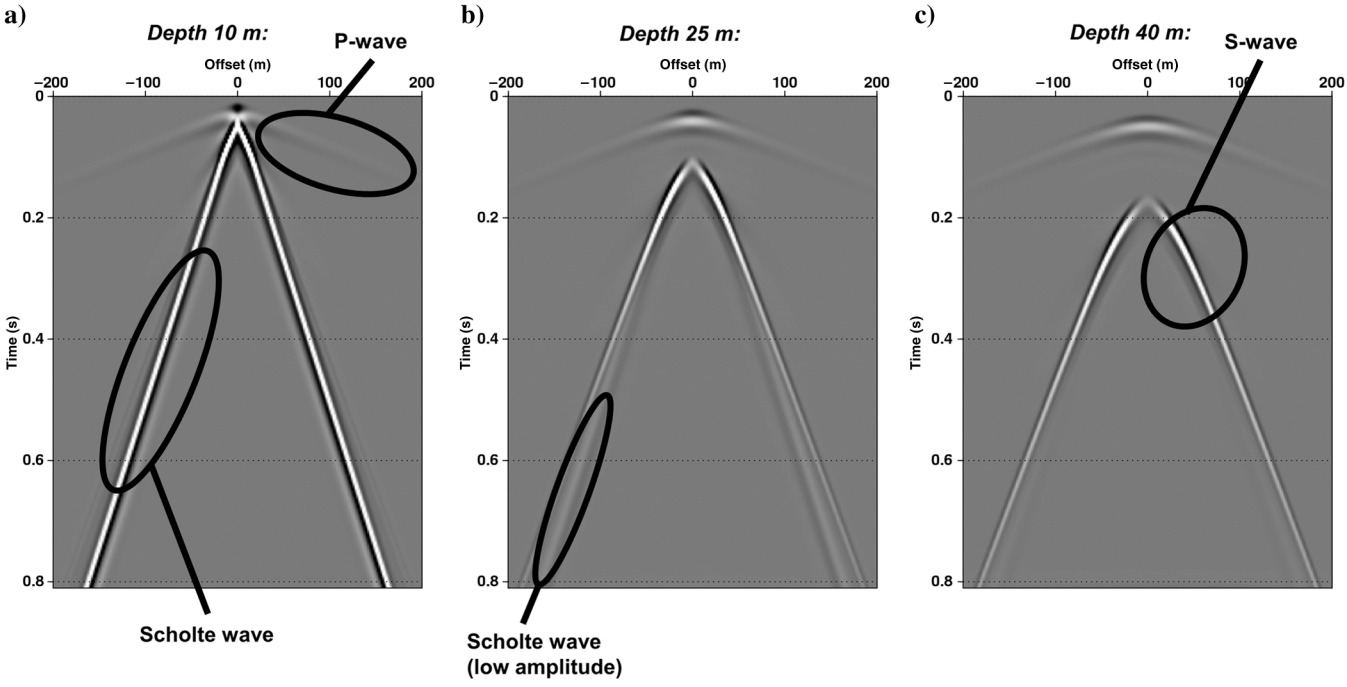

Figure 8. Simulated vertical particle-velocity recording in borehole, using Model 1. Depths: (a) 10 m, (b) 25 m, and (c) 40 m. Events are indicated. (The same clip value is used for all plots).

Figure 9. Simulated particle-velocity recording in borehole using Model 2, including extra time correction for crossline offset of 20 m. Depths: (a) 10 m and (b) 25 m. Note: Scholte wave present at the depth of 10 m, and absent at the depth of 25 m. Plots are equally scaled.

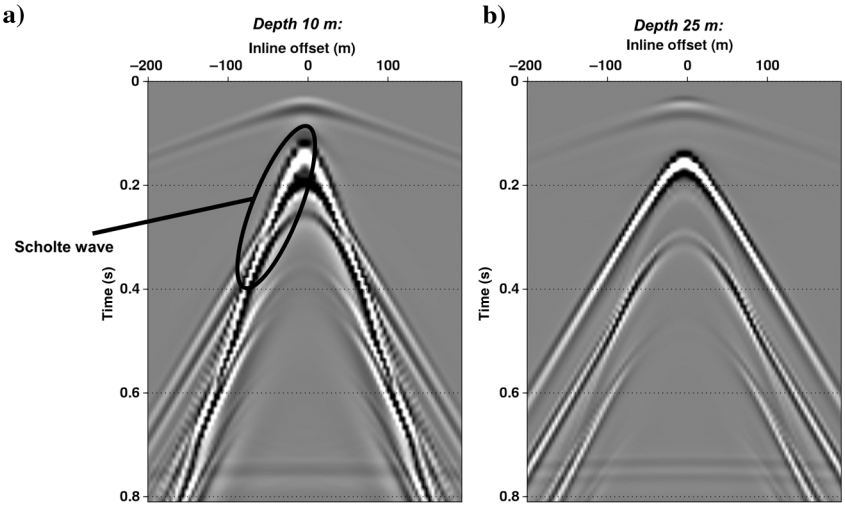

In the left record, the Scholte wave is observed as being the dominant arrival. In the right record, the P*S-wave is well observable as the surface wave is not visible any more. The velocity of the S-wave is now larger and associated with the extra layer in Model 2.

MODELING THE STREAMER DATA

Borehole modeling has shown that a P*S-wave can be generated in the subsurface. However, the situation becomes slightly more complicated when using a streamer. The real streamer data in Figure 1 show evidence of a low shear-related event. This must be due to an evanescent P-wave, but now at the receiver side. Although this may now be obvious, it was not noted in Allouche et al. (2011).

To check this, FD simulations were run again, but with the P-wave source (airgun) and pressure receivers (streamer) in the water. Model 2 was used. As already shown for the borehole data, the extra layer with a faster shear-wave speed creates arrivals comparable to what is seen in the real data (Figure 10). The Scholte wave is dominantly present, but a faster shear-wave arrival is also present and relates to the extra layer in the model.

In looking at the snapshots, it is obvious that these faster events are mainly shear-wave refractions from the layer with the faster shear-wave speed (Figure 11). For clarity, Figure 12 shows a schematic drawing of the geometric and nongeometric paths of the arrival. The angle of the shear wave in the first solid is larger than the maximum angle for which the conventional (geometric) PS-wave occurs; this is therefore a P*S-wave.

As previously stated, the extra layer was added to simulate the real data. The offsets of 30–100 m of the simulated record of Figure 10 can be compared with the real data of Figure 1. Kinematically, the two results show the same behavior, thereby confirming that the faster events in the real data are indeed shear-wave refractions.

This shows that a streamer can detect nongeometrical shear waves when using an airgun source in the water layer, where one relies on an evanescent P-wave at the source and the receiver side.

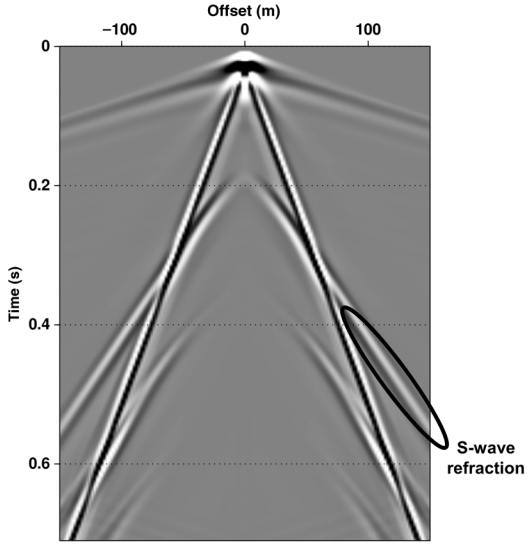

Figure 10. Simulated pressure recording (streamer data) in the water, with P-wave source also in the water, using Model 2.

PROCESSING SYNTHETIC STREAMER DATA FOR REFRACTED SHEAR WAVES

Having established that the faster shear-related events in the real streamer records are shear-wave refractions, the question arises about how these arrivals could be imaged. Of course, the refraction could be treated conventionally, by picking travel times and inverting them for a velocity model, but there are two reasons to choose an approach where the full signal would be used (as in normal reflection processing). First, streamer records are shot from only one side, whereas in refraction seismics, one conventionally prefers to shoot from both sides so that the effect of dipping interfaces can be properly dealt with. Second, the results need to be compared with the processing results for the simultaneously recorded P-wave reflections. The latter can be imaged using normal reflection processing.

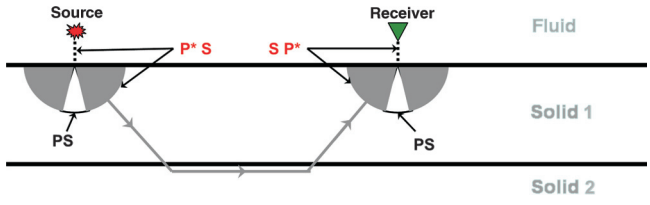

Figure 12. Schematic drawing of snapshots for a streamer for Model 2, showing the path of the nongeometrically converted P*S-wave, at the source and receiver side.

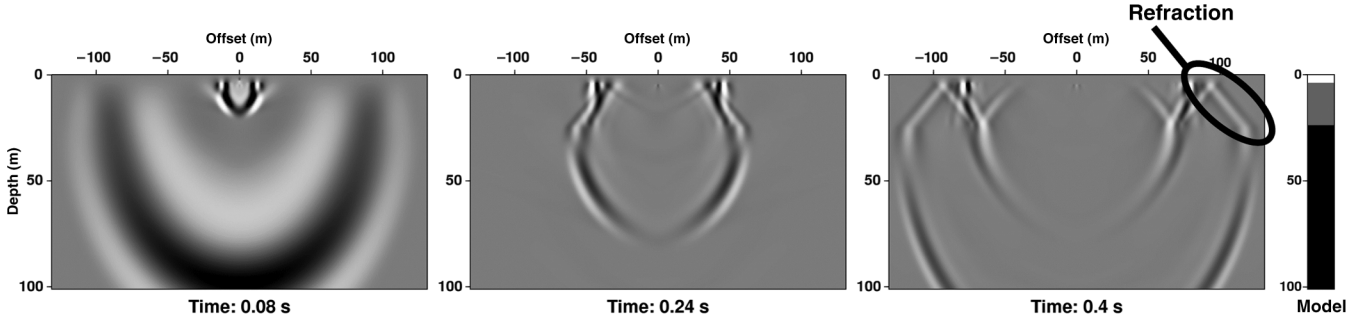

Figure 11. Snapshots of the vertical-stress wavefield τ_{zz} (simulating streamer data in water because at a fluid-solid interface $\tau_{zz} = -p$), with P-wave source in the water, using Model 2. Note the model on the right-hand side where the top (white) indicates the water layer.

Because imaging is not a conventional process for refractions, the approach needed to be tested with numerically simulated data. Such an approach entails some assumptions; one being that the layering is flat, with no dipping interfaces. Structure, however, is very relevant to our real data because faults are present. Therefore we simulated a survey over a fault model and processed the resulting data. The fault is defined at $x = 0$ and only offsets the deeper reflector/refractor; this is shown in Figure 13. As values for the velocities and densities, the same as for Model 2 are taken (see Figure 6).

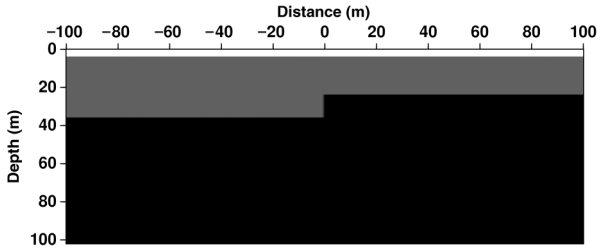

Figure 13. Fault model as used for testing the imaging with refractions. Values of the layers are the same as for Model 2 (see Figure 6).

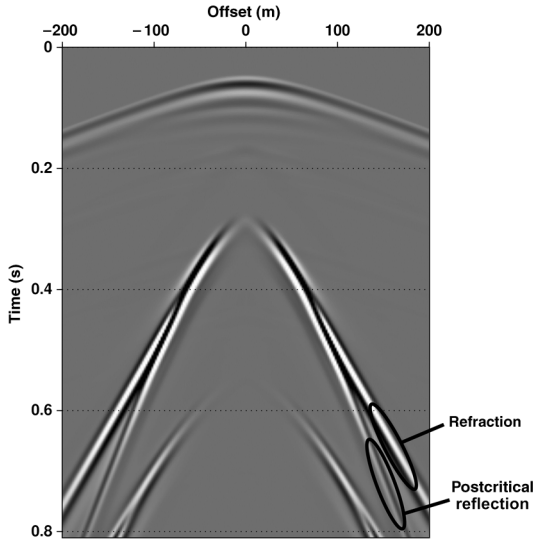

Figure 14. Synthetic shot gather, showing a refracted event but also a postcritically reflected event.

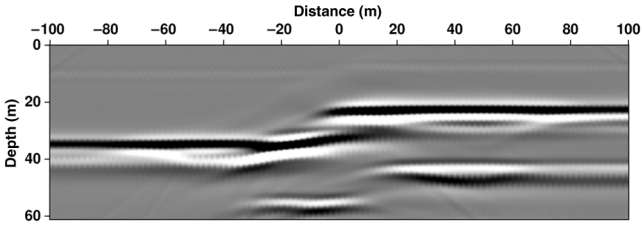

Figure 15. Synthetic data: Depth-converted section from stacked LMO-corrected S-wave refractions; fault at $x = 0$ m. Multiple reflections are also imaged and visible below the first refractor.

The surface/Scholte wave had to be removed from the synthetic data. This was achieved by simulating a homogeneous earth below the water layer, and subtracting these data from the more complicated model. An example of one such synthetic shot is shown in Figure 14. The refracted event is present, but superimposed on it is a slightly curved event, which is interpreted as the postcritically reflected event because the arrival time is the same at the crossover distance and then it deviates from the linear refracted event. There was no attempt to filter this event, instead we relied on CMP stacking to attenuate it. Next, CMP records were created and a linear moveout (LMO) correction applied, after which the CMP data were stacked. These data were subsequently depth-converted, taking into account that the depth conversion for a refracted wave depends on the cosine of the critical in the velocity $T(x = 0) = 2z \cos(\theta_c)/c_{S1}$, where T denotes the traveltime, z the depth of the refractor, θ_c the critical angle and c_{S1} the velocity above the refractor). The result of this processing is shown in Figure 15. For comparison purposes, the simultaneously modeled P-wave reflections were also processed to a final depth image, including migration (Figure 16).

What can be seen in the final shear-wave refraction section is that the shear-wave refractions can be well-imaged at the right depths and lateral position. It can also be observed that the fault transition is not as perfect as imaged with the P-wave reflections, but the results are nonetheless good. It is acknowledged that an approach using the concepts of seismic migration would have been ideal, but it is beyond the scope of this article. Therefore, the above-described pragmatic approach has been adopted here. We used this approach with the real streamer data as described next.

PROCESSING STREAMER DATA FOR REFRACTED SHEAR WAVES

In this section, the steps of processing the streamer data for imaging the shear-wave refractions are described (Table 1). The first step is the assignment of GPS coordinates to the source. The receiver coordinates were then defined relative to them. Because of the irregularities in the speed of the boat, the source positions and associated data needed to be regularized. First, high-cut filtering was used to remove the P-wave reflections (they were processed separately), and dip-filtering to remove the Scholte wave. Because the wavelet appeared "ringy" (Figure 1), a prediction-error filter was also applied. Regularization of the source coordinates (by linear interpolation) was then performed for each receiver.

The next steps were specific to the refracted arrival events. After analysis of the full data set, two refracted events were identified, with velocities of 400 m/s and 600 m/s. In some CMP gathers, these two events intersect (Figure 17). Because of this intersection,

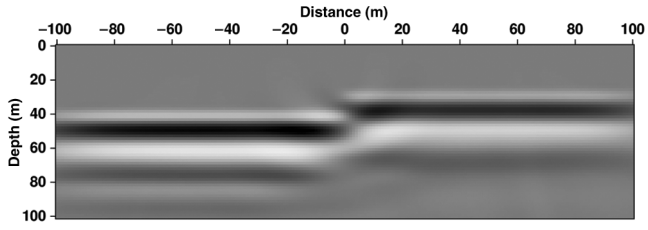

Figure 16. Synthetic data: Depth section of P-wave reflectors, using a conventional normal moveout, stack, migration, and depth-conversion approach ($V_{rms} = 1600$ m/s); fault at $x = 0$ m.

it was decided to decompose the data into two subsets, one containing the linear event of 400 m/s and the other the remaining data (including the linear event of 600 m/s) (Figure 17). Each subset was then separately processed: An LMO correction was applied, and the CMP data were stacked and subsequently depth-converted, taking into account that a refraction has an intercept time that is $2z\cos(\theta_c)/c_{S1}$. Here, it is assumed that there is only one layer on top of the refractor. The velocity c_{S1} is the shear-wave velocity of the first layer, i.e., 274 m/s (derived from the Scholte-wave velocity of 240 m/s, assuming a P-wave velocity of 1600 m/s and a density of 1500 kg/m^3). The resulting depth section for each of the events is shown in Figure 18. Because the resulting wavelet still looks to be ringing, one could again apply a prediction-error filter, which is sometimes done in standard practice, but the results were

Table 1. Processing steps for imaging shear-wave refractions.

Process	Aim
GPS processing	Assign absolute source coordinates and relative receiver coordinates
High-cut filtering	Remove high-frequency P-wave reflections
Slow-wave dip-filtering	Remove Scholte wave
Prediction-error filtering	Remove ringing of (shear-wave related) wavelet
Regularization of source coordinates in common-receiver domain	Obtain regular spacing for CMP-based processing
CMP-binning	Allow for CMP-based processing
Decomposition of different refracted-wave arrivals, via dip-filtering, based on different velocities	Allow different LMO corrections for different refractions
For each refracted-wave arrival: • LMO correction • CMP-stack • Depth conversion	Obtain depth sections from different refractions.
Summation of different depth-converted shear-wave-stacks	Obtain final imaged depth section (comparable to depth section of P-wave reflectors)

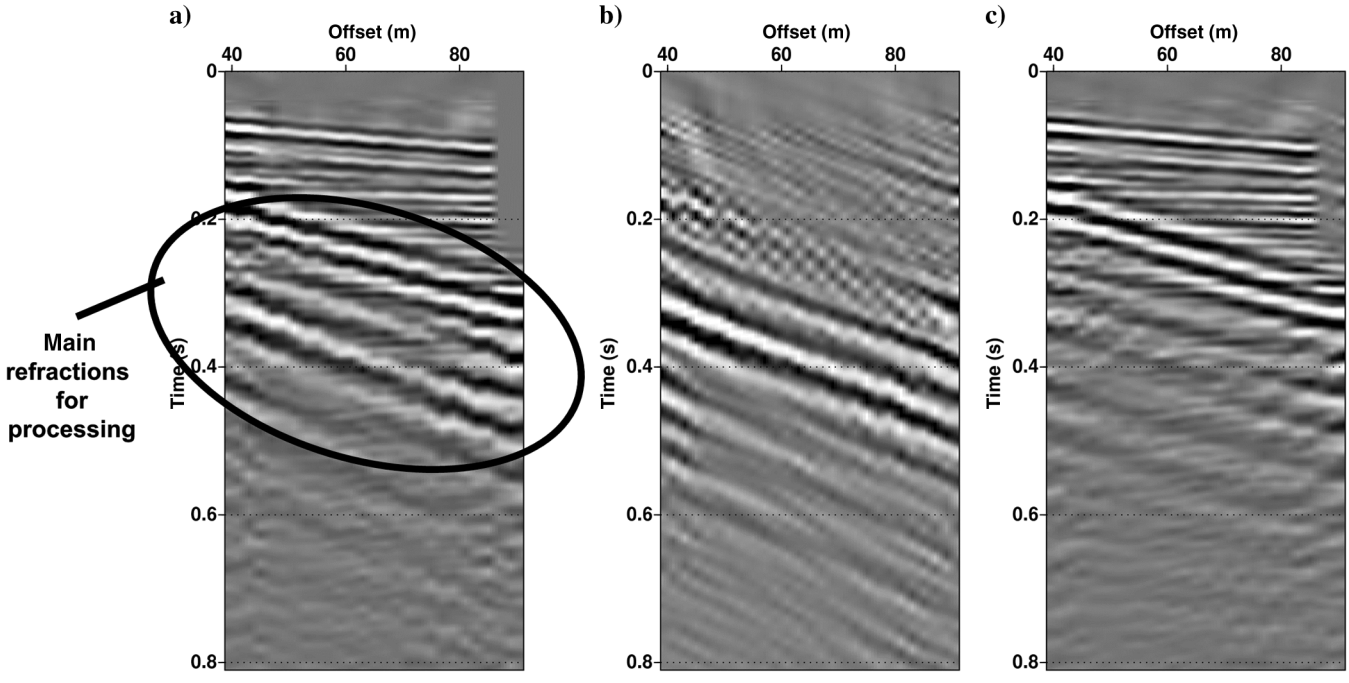

Figure 17. Separation of different refracted events in real data as indicated. (a) Original CMP, (b) slow events retained, and (c) fast events retained. Full data retained after separation: $(a) = (b) + (c)$.

not better overall, so we omitted the extra prediction-error filtering. As the final step, the two depth-converted substacks were summed, resulting in the final section at the bottom of Figure 18.

Before highlighting some characteristics of the shear-wave sections, it is very important to take into account the P-wave reflectivity data that were recorded simultaneously with the shear-wave data. The P-wave reflectivity is mainly contained in the high-frequency part. These data were processed with a conventional P-wave processing sequence (including poststack migration) using a constant velocity of 1600 m/s, which seemed good enough for these data. The resulting P-wave-reflectivity depth section is shown in Figure 19.

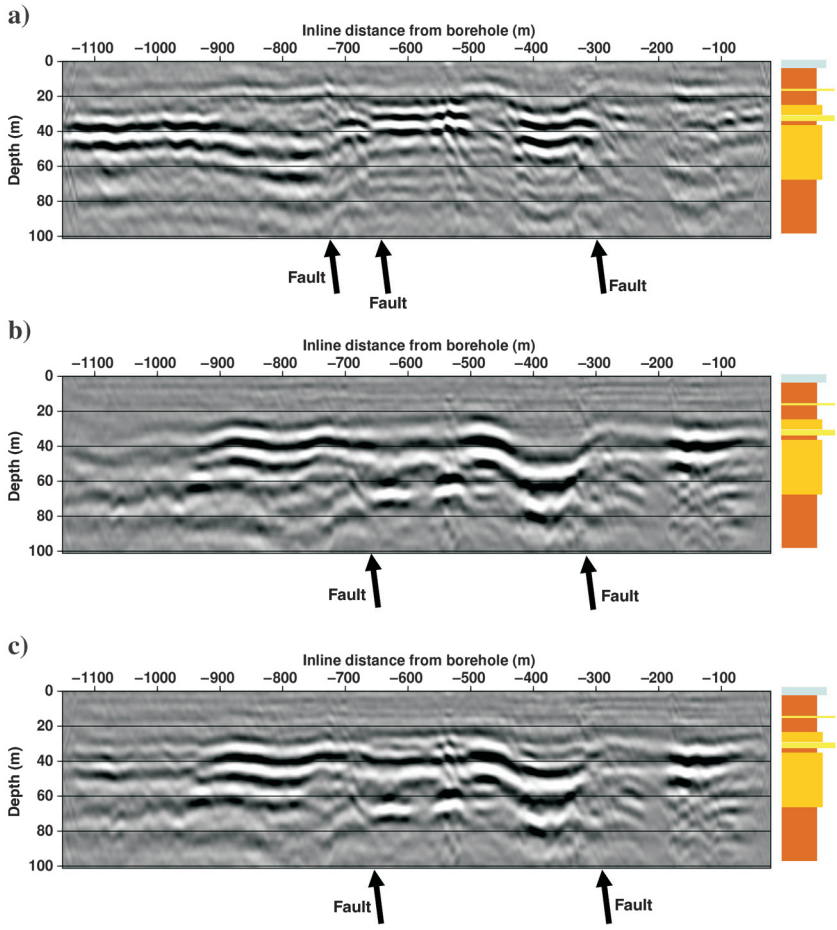

Figure 18. Depth sections for shear-wave refracted events of (a) 400 m/s, (b) 600 m/s, and (c) the sum of (a) and (b). The simplified lithological column described in Figure 3 is next to each section.

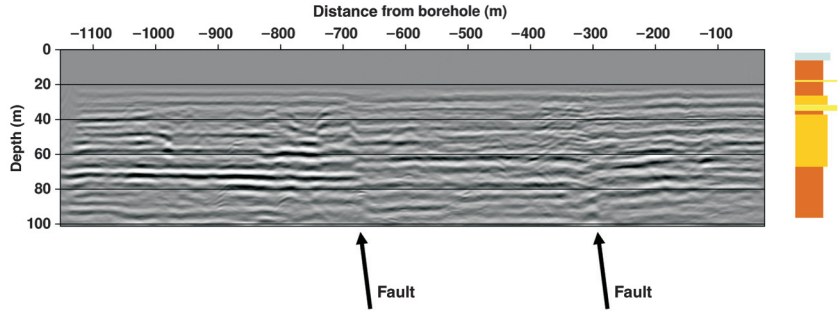

Figure 19. Conventionally processed P-wave section (with poststack migration and depth-conversion). The lithological column described in Figure 3 is next to this section. Two interpreted fault locations are indicated.

EVALUATION OF RESULTS

When looking at the results, some lateral changes can be observed in the stacked sections. Let us first focus on the conventional P-wave section (Figure 19). In that section, two main faults or fault systems can be detected. The first one is around $x = -320$ m. The other one is around $x = -680$ m, with a possibly smaller one around $x = -730$ m. Next to these faults, some lateral changes in amplitude occur, such as near $x = -980$ m and $x = -150$ m.

When looking at the shear-wave sections (Figure 18), the fault system can also be easily observed. The fault at around $x = -320$ m is clear, in the summed section (Figure 18c) and in the individual low-event and fast-event refraction sections (Figure 18a and 18b, respectively). The fault near $x = -680$ m is easily observable in the summed section, but it is very abrupt, especially in the section of the slow (400 m/s) event. Also, the possibly smaller fault at $x = -730$ m is abrupt in the slow-event section. In the fast-event section, the fault is not so observable and therefore also not so distinct in the summed section either.

When comparing the end of the sections with the borehole data, it can be seen that the refractor of 400 m/s (see Figure 18a) correlates well with the thin layer in the borehole at a depth of around 16 m. The refractor of 600 m/s (see Figure 18b) correlates well with the layer boundary at a depth of around 23 m. When looking at the P-wave reflection section, the 23-m depth event is visible, whereas the event at 16 m is too shallow to be imaged. The P-wave section also shows some deeper reflectors that are not reached by the refractions in the shear-wave section.

When comparing the S-wave section(s) with the P-wave section, similarities and differences can be observed. From shallow seismic experiences on land, this is commonly observed and then we are not considering an S-wave section of refractions which is expected to resemble even less. Starting at the left of the sections between $x = -1150$ m and $x = -900$ m, the S-wave refractor at around 35 m depth can be seen in the S-wave and the P-wave section. At around $x = -950$ m, the same event looks laterally discontinuous in amplitude (but still continues) which, after some inspection, can also be observed in the P-wave section. At around $x = -520$ m, a lateral change is observable in the S-wave section which can also be seen in

the P-wave section but is not so clear. Between $x = -400$ m and $x = -300$ m, a sag in the S-wave section can be seen which is not present in the P-wave section; we cannot explain this difference. Near the borehole, the S-wave and the P-wave section show the boundary at around 23 m.

Laterally, the S-wave section has more variation than the P-wave section, but this is expected because changes in shear-wave properties in shallow soils are generally larger than P-wave properties (also look at the relative variations in seismic velocities in Figure 6 to appreciate this). This is particularly true in saturated soft soils where P-waves are ruled by the water, whereas S-waves are ruled by the solid matrix. This is known from shear-wave reflectivity sections on land (Ghose et al., 2004). What can also be observed is that the shear-wave sections give results at shallower depths than the P-wave sections, as is well-known from shear-wave seismics on land. A comparison with the P-wave section shows that the depth resolution for the P-waves is still better than for the shear waves. That the resolution is less for shear waves, which is contrary to what is often obtained on land, may well have to do with that the attenuation is higher for higher frequencies due to the evanescent-wave path in the water. However, it should be realized that the shear-wave information is obtained with the same survey, so the shear-wave information should be seen as additional to the P-wave reflectivity information. And, for many civil applications, shear-wave properties are usually more important for subsurface characterization than P-wave properties, so a combination of the P- and S-wave sections is very powerful indeed.

DISCUSSION

The above results are very promising, but one should be aware that the approach described in this paper can only be used under certain circumstances. The most important one is that the distance between the water bottom and the seismic source and receivers must be within a quarter of the dominant wavelength for the P-wave. This circumstance was satisfied during our experiment. However, when the water bottom varies significantly in depth, it may be difficult to maintain the water bottom in the near field of the source and/or streamer.

Further effort in future surveys should be put on spatial sampling. In our survey, the boat speed could be reduced to $\sim$1 m/s by sailing against the current, which had a speed of $\sim$4 m/s. This resulted in a good source spacing; such favorable circumstances may not always be the case. In such cases, a fixed frame for the source and streamer may be needed to reduce the effect of the water flow.

In our survey, a standard streamer with a hydrophone-group spacing of 3.125 m was used. However, this group spacing is rather large compared with that used for geotechnical shear-wave seismics on land. There, spacings of 2 and 1 m are often used. Also, with our streamer the offsets were optimized (30–100 m), whereas other shorter offsets may be needed. Shorter offsets would especially aid in the interpretation of events, such as the direct waves and earlier refracted events. A streamer with 48 groups at spacings of 2 m would have been much better than the one we used. It would also have allowed better processing.

A final remark must be made with regard to the underlying assumptions made in our refraction-processing approach. Horizontal layering is assumed, but often this assumption is unwarranted; dipping refractors exist in many cases. To deal with this problem, one can sail with the boat in both directions. An additional possibility, which is always preferable from a purely technological point of view, is to include measurements from a borehole and use the velocities from the borehole. In any case, boreholes are often desirable for shallow investigations for validation purposes.

CONCLUSIONS

It is well known that streamers can record S-wave energy that converts to P at the water bottom, albeit with a small transmission coefficient. In this article it is shown that marine streamer data can also be used to obtain nongeometrical shear body wave information. In our case, shear-wave could be retrieved from streamer data. Via field experiments and modeling, it is shown that nongeometrical shear waves are recorded via an evanescent compressional wave in the water, on the source and on the streamer side. To pick up this energy, it is assumed that the source and the receivers are near (less than a quarter of the dominant wavelength of the P-wave) to the water bottom.

This approach is validated via an experiment in the river Danube south of Budapest, Hungary. To show that the shear-related arrivals were body waves rather than surface waves, a borehole was drilled and used for multicomponent recordings. The borehole data showed that the shear waves were indeed propagating as body waves. The borehole data also show that the arrivals in the streamer data were mainly refracted shear waves. Numerical modeling supports this interpretation.

The streamer data were subsequently processed to obtain a shear-wave refraction section. The full signal was used, as is common in reflection-data processing. The Scholte-wave arrival was removed, the wavefield decomposed into different refracted arrivals, LMO-corrected, stacked, and depth-converted for each refracted arrival before the different depth sections were added together. The obtained S-wave-refraction section was compared with the standard P-wave reflection section and the comparison showed that our approach has the power to obtain refracted shear-wave sections from streamer data, in addition to conventional P-wave reflectivity sections.

ACKNOWLEDGMENTS

The support from the Department of Geophysics, Eötvös Loránd University (ELTE), Budapest, Hungary, is very much appreciated, in particular Frank Horváth, Deák Attila, and Kudó István. In addition, Willem Versteeg from Ghent University, Belgium, is gratefully acknowledged for his advice and support. Alber Hemstede from Delft University is acknowledged for enthusiastic technical support. Finally, we thank the reviewers for all their suggestions for improving the text.

REFERENCES

Allouche, N., G. G. Drijkoningen, W. Versteeg, and R. Ghose, 2011, Converted waves in a shallow marine environment: Experimental and modeling studies: Geophysics, **76**, no. 1, T1–T11, doi: 10.1190/1.3511524.

Allouche, N., G. G. Drijkoningen, W. Versteeg, and D. G. Simons, 2008, Studying converted waves in shallow marine environment: Proceedings of the European Conference of Underwater Acoustics, 369–374.

Allouche, N., J. V. D. Neut, and G. G. Drijkoningen, 2010, Methodology for dense spatial sampling of multicomponent recording of converted waves in shallow marine environments: Geophysics, **75**, no. 6, J29–J37, doi: 10.1190/1.3496001.

Bada, G., and F. Horváth, 2001, On the structure and tectonic evolution of the Pannonian basin and surrounding orogens: Acta Geologica Hungarica, **44**, 301–327.

Caiti, A., A. Akal, and R. D. Stoll, 1994, Estimation of shear wave velocity in shallow marine sediment: IEEE Journal of Oceanic Engineering, **19**, 58–72, doi: 10.1109/48.289451.

Csontos, L., and A. Nagymarosy, 1998, The mid-Hungarian line: A zone of repeated tectonic inversion: Tectonophysics, **297**, 51–71, doi: 10.1016/S0040-1951(98)00163-2.

Daley, P. F., and F. Hron, 1983, Nongeometric arrivals due to highly concentrated sources adjacent to plane interfaces: Bulletin of the Seismological Society of America, **73**, 1655–1671.

Dombrádi, E., D. Sokoutis, G. Bada, S. Cloetingh, and F. Horváth, 2008, Quaternary inversion of the Pannonian lithosphere: Large-scale lithospheric folding controlling active deformation and topography development: Bollettino di Geofisica Teorica ed Applicada, **49**, 38–42.

Drijkoningen, G. G., and C. H. Chapman, 1988, Tunnelling rays using the Cagniard-de Hoop method: Bulletin of the Seismological Society of America, **78**, 898–907.

Ghose, R., and J. Goudswaard, 2004, Integrating S-wave seismic-reflection data and cone penetration test data using a multiangle multiscale approach: Geophysics, **69**, 440–459, doi: 10.1190/1.1707064.

Kaufmann, R. D., J. Xia, R. C. Benson, L. B. Yuhr, D. W. Casto, and C. B. Park, 2005, Evaluation of MASW data acquired with a hydrophone streamer in a shallow marine environment: Journal of Environmental and Engineering Geophysics, **10**, 87–98, doi: 10.2113/JEEG10.2.87.

Park, C., R. D. Miller, and J. Xia, 1999, Multi-channel analysis of surface waves: Geophysics, **64**, 800–808, doi: 10.1190/1.1444590.

Park, C. B., R. D. Miller, J. Xia, J. Ivanov, G. V. Sonnichsen, J. A. Hunter, R. L. Good, R. A. Burns, and H. Christian, 2005, Underwater MASW to evaluate stiffness of water-bottom sediments: The Leading Edge, **24**, 724–728, doi: 10.1190/1.1993267.

Roth, M., and K. Holliger, 2000, The non-geometric $\bar{P}$ S-wave in high-resolution seismic data: Observations and modelling studies: Geophysical Journal International, **140**, F5–F11, doi: 10.1046/j.1365-246x.2000.00030.x.

Thorbecke, J. W., and D. Draganov, 2011, Finite-difference modeling experiments for seismic interferometry: Geophysics, **76**, no. 6, H1–H18, doi: 10.1190/geo2010-0039.1.

Virieux, J., 1986, P-SV wave propagation in heterogeneous media: Velocity-stress finite difference method: Geophysics, **51**, 889–901, doi: 10.1190/1.1442147.